

Molecular Trapping Strategy To Stabilize Subnanometric Pt Clusters for Highly Active Electrocatalysis

Wenya Zhang,^{†,‡} Qishi Yao,[§] Gaopeng Jiang,[†] Chun Li,[‡] Yongsheng Fu,^{*,‡} Xin Wang,[‡] Aiping Yu,^{*,†} and Zhongwei Chen^{*,†}

[†]Waterloo Institute for Nanotechnology, University of Waterloo, Waterloo, Ontario N2L3G1, Canada

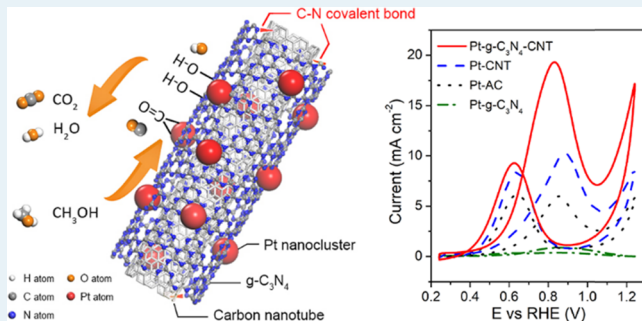
[‡]Key Laboratory of Soft Chemistry and Functional Materials, Nanjing University of Science and Technology, Ministry of Education, Nanjing 210094, China

[§]Department of Physics, Southern University of Science and Technology, Shenzhen 518055, China

S Supporting Information

ABSTRACT: Structure engineering is an effective way to substantially adjust the chemical and physical properties of materials. However, the effects of structure engineering of carbon hosts on the catalytic properties of Pt-based catalysts at the molecular scale are poorly understood. Herein, we report a molecular-level strategy to anchor and stabilize subnanometric Pt clusters on a covalently coupled host of graphitic carbon nitride ($\text{g-C}_3\text{N}_4$) and carbon nanotubes (CNT) for the development of electrocatalysts with high activities toward methanol oxidation reactions. Theoretical evaluation and experimental validation identified that the chemical integration of $\text{g-C}_3\text{N}_4$ on CNT is critical in optimizing the electronic structures and catalytic properties of Pt catalysts. As a result, the Pt-g-C₃N₄-CNT possesses a high energy level of *d*-band position, significantly strengthening its adsorption behaviors for the key reaction intermediates during the methanol electrooxidation process and energetically decreasing the energy barriers in the multistep reaction pathways. Combining with the strong catalyst–support interactions afforded by the adaptive coordination environment of $\text{g-C}_3\text{N}_4$ with Pt clusters as well as the unimpeded electron transfer via a σ -orbital overlap between CNTs and $\text{g-C}_3\text{N}_4$, the as-obtained Pt-g-C₃N₄-CNT possesses prodigious electrocatalytic properties including high activities, unusual poison tolerance, and reliable long-term discharge stabilities toward methanol oxidation reactions, in comparison to commercial Pt/activated carbon (Pt-AC) and Pt-CNT catalysts. This molecular-level finding opens up a new avenue to design and develop more efficient and effective carbon-based supports for fabricating advanced heterogeneous catalysts and could also be extended to more applications, such as lithium-ion batteries, lithium-sulfur batteries, supercapacitors, and sensors.

KEYWORDS: subnanometric Pt clusters, structure engineering, graphitic carbon nitride nanotube, covalent coupling, methanol oxidation



Heterogeneous catalysis is a surface process involving most, if not all, constitutional atoms at or near the catalyst surface.^{1–3} For noble metal catalysts, the nanostructures of metal clusters with dimensions in the range of a single metal atom to the nanoparticles (>2 nm) have gained great interest in order to lower the cost of the catalysts and exploit efficient use of catalytically active components.^{4,5} For instance, Pt-based catalysts possess unique and significant electrocatalytic activities toward methanol oxidation reactions, but the high costs and the scarcity of Pt sources seriously block their large-scale commercial applications.^{6,7} Small nanoclusters are therefore extremely desirable in improving Pt utilization efficiency. Generally, the size of metal clusters is also one of the most critical factors that dictate the performances of a catalyst.³ Subnanometric Pt clusters have sizes approaching the electron's Fermi wavelength (ca. 0.7 nm), leading to

molecule-like properties including discrete size-dependent electronic states and energy levels.^{8,9} It offers promise of facilitating kinetics toward methanol electrooxidation by substantially whittling the oxygen-containing reaction intermediate absorption to some extent. By downsizing the clusters, the number of surface atoms exposed profoundly increases where these low-coordination, unsaturated atoms function as active sites, leading to a magnitude higher specific catalytic activity.^{10,11} However, fabrication of practical and stable subnanometric catalysts remains a considerable challenge because, typically, such metal clusters are spontaneously liable to aggregate and particle grows under realistic reaction

Received: July 15, 2019

Revised: October 31, 2019

Published: November 6, 2019

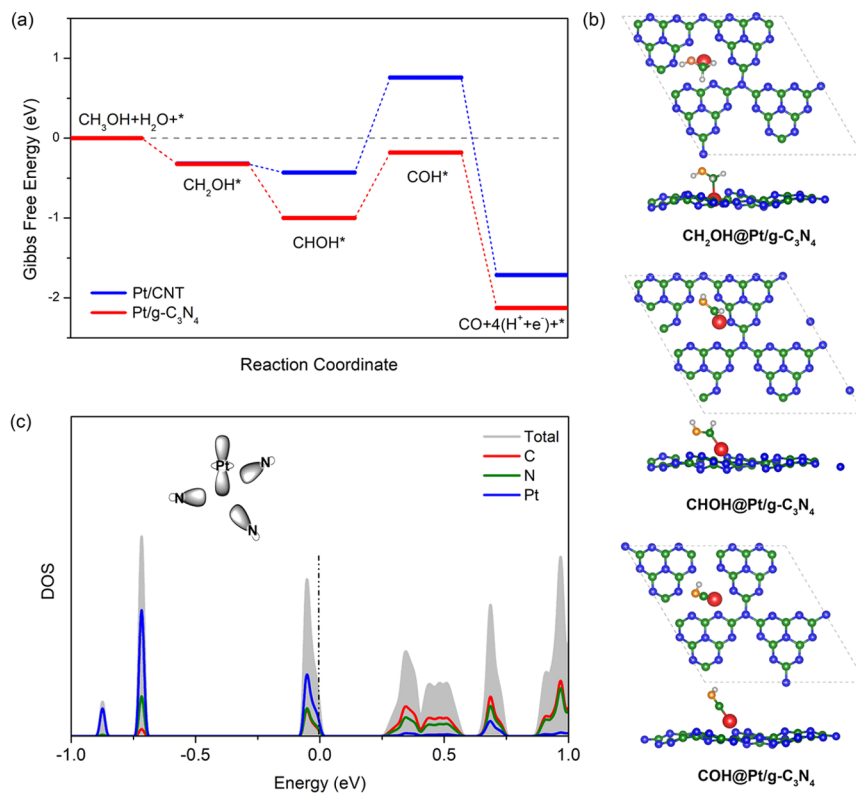


Figure 1. (a) Free energy diagram of methanol oxidation reaction on Pt/CNT and Pt-g-C₃N₄. (b) Top and side views of atomic configurations of the intermediate states during methanol oxidation reactions. Red, green, gold, blue, and white represent Pt, C, O, N, and H atoms, respectively. (c) Partial density of states (PDOS) plots are shown for Pt-g-C₃N₄; the Fermi energies are all normalized at $E = 0$. The inset in panel (c) illustrates a schematic representation of electronic structures of the Pt atom on the g-C₃N₄ substrate.

conditions.¹² A popular solution entails the use of suitable supports, to which the highly mobile metal can be anchored. Efforts have been made to preferentially locate the framework of Pt clusters in MFI zeolites,¹³ which could sufficiently stabilize these subnanometric metal clusters serving as the ideal supports. However, it still remains a big challenge to localize the subnanometric metal clusters on a specific site and hence modulate their reactivities.

Mesoporous polymeric graphitic carbon nitride ($\text{g-C}_3\text{N}_4$) is an emerging, powerful class of two-dimensional substrates for firmly trapping ultrasmall clusters owing to its lattice-hole structure. The material, in fact, contains periodic tri-*s*-triazine subunits coupled via the planar tertiary amino groups, resulting in uniform structural N-coordinating cavities.^{14–16} The high level of pyridinic nitrogen in each cavity is capable of tenaciously capturing metal ions owing to the nature of abundant electron lone pairs.^{17–19} Such strong electronic interactions have extensively been regarded as a crucial tool to manipulate the electronic structures of the metal nanoclusters and thus to interact with the intermediates during the catalytic reactions.^{11,17} More importantly, $\text{g-C}_3\text{N}_4$ offers abundant and homogeneous nitrogen coordinators, which gives rise to many inherent advantages, including sustaining metal atoms with their neutral states,¹⁰ efficiently accumulating surface polarization charges on metal atoms,^{20,21} and affording more accurate information for the identification of catalytically active sites.^{11,17,22} Unfortunately, its low electrical conductivity dramatically deteriorates the electrocatalytic processes, limiting their applications in the field of electrochemistry. Tremendous efforts have been made in exploring effective strategies to improve its electron transferability, such as designing advanced

nanostructures,^{23,24} incorporating mesoporous structures,^{25,26} combining with carbon materials,^{7,27–29} and heteroatom doping.^{30,31} However, developing a strongly coupled $\text{g-C}_3\text{N}_4$ -based composite support with fast electron mobility, robust structural stability, and mechanical strength is still highly desirable.

In this work, the newly realized covalently coupled $\text{g-C}_3\text{N}_4$ -modified carbon nanotubes ($\text{g-C}_3\text{N}_4$ -CNT) was investigated as a platform to stabilizing a large number of highly-dispersed, long-term stable Pt clusters with subnanometric size (~ 1.0 nm). The strong catalyst–support interactions afforded by the adaptive coordination environment of $\text{g-C}_3\text{N}_4$ with Pt clusters and the unimpeded electron transfer via a σ -orbital overlap between the $\text{g-C}_3\text{N}_4$ and CNT simultaneously lead to significant enhancement of Pt's catalytic performances. As a proof of concept, the resulting Pt-g-C₃N₄-CNT composite was theoretically predicted and experimentally measured as an efficient and effective catalyst toward the methanol oxidation reactions for application in the direct methanol fuel cell (DMFC). A combination of density function theory (DFT) calculations and electrochemical studies confirmed that the Pt-g-C₃N₄-CNT possesses a more appropriate *d*-band position and thus is more energetically favorable for methanol electrooxidation than the Pt/carbon nanotubes (Pt-CNT), and the stronger binding of OH* on $\text{g-C}_3\text{N}_4$ enables the easier removal of the poison intermediate of CO*. Consequently, the Pt-g-C₃N₄-CNT exhibits outstanding electrocatalytic performance, for instance, large electrochemically active surface areas, unusual poison tolerances, high power densities, and reliable discharge stabilities, which is remarkably outperformed than the commercial Pt/activated carbon (Pt-AC) and Pt-CNT.

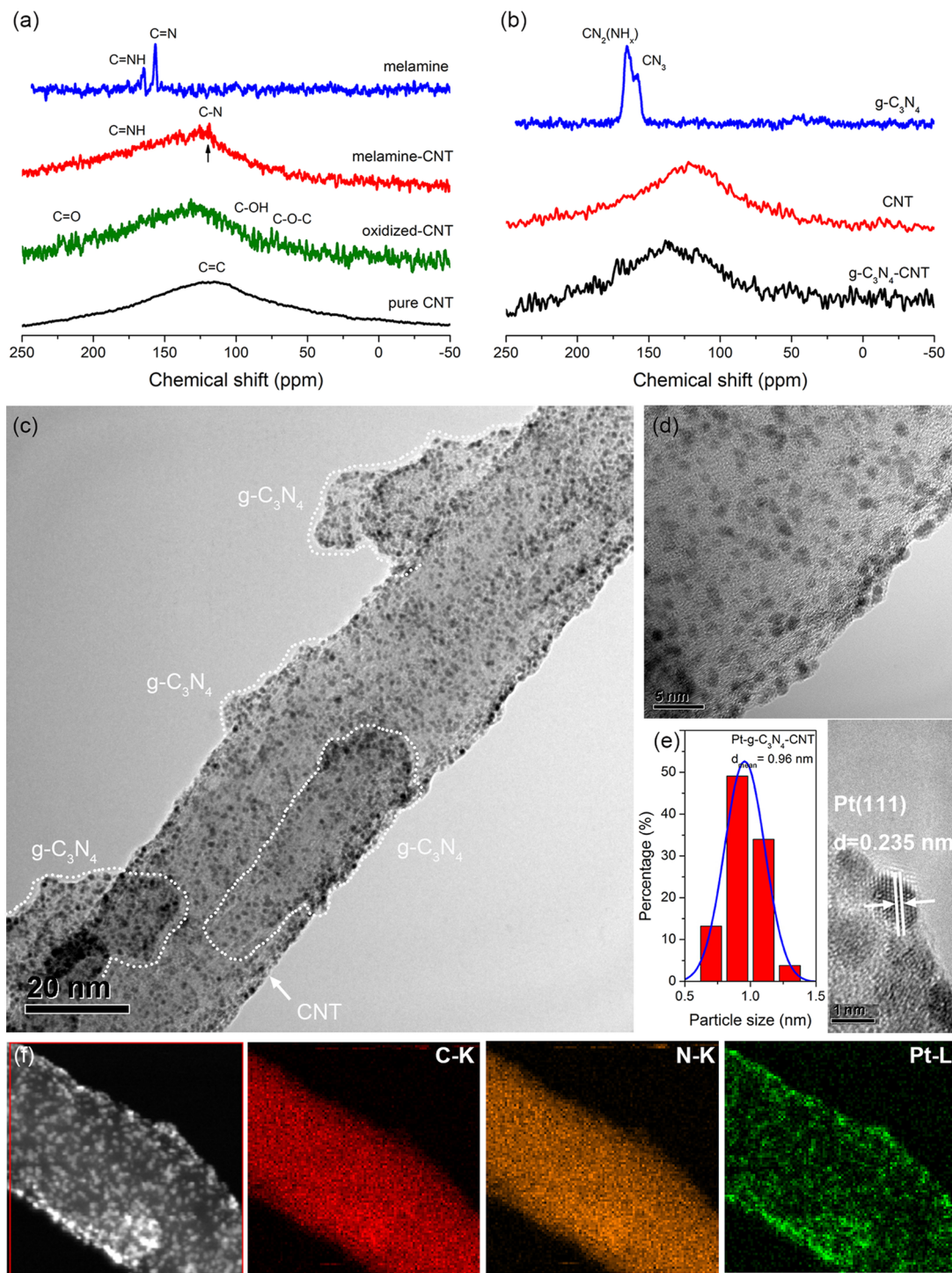


Figure 2. Solid-state ^{13}C MAS NMR spectra of (a) pure CNT, oxidized CNT, melamine-CNT, and melamine, and (b) g-C₃N₄-CNT, CNT, and g-C₃N₄. (c,d) Typical TEM images of Pt-g-C₃N₄-CNT. (e) High-resolution TEM image and the Pt nanoparticle size distribution of Pt-g-C₃N₄-CNT. (f) HAADF-STEM image of Pt-g-C₃N₄-CNT and the EELS elemental maps of C, N, and Pt.

First, the effects that the supports of g-C₃N₄ and CNTs have on Pt atoms' adsorption, migration, and catalytic mechanisms on the methanol oxidation reaction were investigated. Figure S1 shows the optimized geometry structures of Pt on g-C₃N₄ and CNTs. We theoretically evaluated their performance as anodes in DMFC by calculating the free energy diagram for methanol oxidation reactions taking the computational hydrogen electrode (CHE) method.^{32,33} The stepwise dehydrogenation of methanol on Pt atoms undergoes an indirect way,

namely, $\text{CH}_3\text{OH} \rightarrow \text{CH}_2\text{OH}^* \rightarrow \text{CHOH}^* \rightarrow \text{COH}^* \rightarrow \text{CO}^*$, followed by oxidative removal of the absorbed CO* via surface accumulated hydroxyl (OH*), which are consistent with the previous study.³⁴ The Gibbs free energies of the pathways during the methanol oxidation reaction on both Pt-g-C₃N₄ and Pt-CNT are shown in Figure 1a, and the detailed structures of the intermediates are displayed in Figure 1b and Figures S2 and S3. All the reaction steps are downhill thermodynamically, with the exception of dehydrogenating from the O–H bond,

which can be considered as the rate-determining step of the overall reactions (Table S1). In comparison with that of Pt-CNT, the intermediates bind more strongly on Pt-g-C₃N₄, especially for the rate-determining step, suggesting as more energetically favorable, thus demonstrating a higher reactivity. Moreover, the formation of OH* by water dissociation is more easily activated on g-C₃N₄ than CNTs, which is able to efficiently facilitate the removal of poisoning CO*.

Partial density of states, known as PDOS, upon adsorption of Pt on g-C₃N₄ and CNTs was also conducted to assess their stability during catalytic reactions. The clear overlap lying on the position of Fermi energy $E = 0$ in the PDOS of Pt-g-C₃N₄ in Figure 1c reveals a much stronger interaction between g-C₃N₄ and Pt than that of Pt-CNT as shown in Figure S4. This interaction springs from the coordinating ability of N atoms with Pt atoms via constituting *d-p* dative (dipolar) bonds, as organometallic complexes.³⁵ Such a phenomenon plays a critical role in tethering sizable Pt clusters and preventing them from migration and agglomeration. Further examination of the *d*-band center based on the PDOS analyses was figured subsequently, determined to be -1.35 eV for Pt-g-C₃N₄ and -1.67 eV for Pt-CNT. Qualitatively, a higher *d*-band position leads to a closer *d*-center to the Fermi level, which is of electronic origin, and gives a supplementary explanation of higher reactivity.^{36,37}

Proof-of-concept studies were conducted to anchor Pt clusters on g-C₃N₄ as an advanced anode material for methanol electrooxidation, and CNTs were involved by an *in situ* chemically integrated approach to improve the electronic conductivities and gain the accessible catalytically active sites. Briefly, commercial multiwalled CNTs (CAS Chengdu Organic Chemistry Co., Ltd.) were first functionalized via a modified Hummers method. The oxidation steps were considered to involve oxygen-containing groups on the sidewalls of CNTs. After that, the oxidized CNTs were reacted with melamine to fabricate an intercoupling CNT-melamine composite coupled by covalent C–N bonds. Then the nitric acid solution was added to induce the supramolecular behavior of protonated melamine to form an ordered nanobelt attached on CNTs. The as-resulting product was thermally treated at 350 °C, and the protonated melamine nanobelt tends to *in situ* polymerized into a g-C₃N₄ nanotube wrapped on CNTs. Subsequently, the as-obtained g-C₃N₄-CNT acts as the supporting material for the nucleation and growth of highly uniform Pt nanoparticles via a soft chemistry method.

Evidence for the formation of the supramolecular complex is provided by X-ray powder diffraction (XRD) analysis as well as Fourier transform infrared (FT-IR) spectroscopy (Figure S5). The appearance of new peaks in XRD patterns and the shift of the tri-*s*-triazine ring vibration in FT-IR confirm the creation of a new arrangement via hydrogen bonds in the protonated melamine supramolecular, which shows a nanobelt morphology, as depicted in Figure S6. After being thermally treated, a distinct tubular like structure with a diameter of ~150 nm and a length of ~10 μm can be observed (Figures S7 and S8), in agreement with the reported g-C₃N₄ nanotube.³⁸ The rolling or curling behavior of this protonated melamine at elevated temperature is driven by the thermodynamic phenomenon of surface free energy minimization, which is familiar with the formation of tubular organic, for instance, polyaniline nanotube.³⁹ Further, an *in situ* chemical synthesis approach was designed to grow g-C₃N₄ nanotubes on the surface of CNTs, fabricating strongly coupled g-C₃N₄-CNT composites with fast

electron mobility and robust structural stability. The formation process and the chemical structures of g-C₃N₄-CNT were investigated by solid-state NMR spectroscopy (Figure 2a,b). In detail, the ¹³C MAS NMR spectrum of pure CNTs shows a broad peak centered at 129.2 ppm, ascribed to the sp²-hybridized carbon of the graphene network in their intrinsic structure. After being oxidized, three well-resolved peaks at 58.9, 69.1, and 228.1 ppm arise up in oxidized-CNT, which can be attributed to the ¹³C nuclei in epoxy, hydroxyl, and carbonyl groups, respectively,^{40–42} indicating the successful incorporation of the oxygen-containing groups on the sidewalls of CNTs. As for that of melamine, the signals located at 158.8 and 167.5 ppm are attributed to the sp and sp² carbons. We note, inspirationally, that a very well developed resonance, the shoulder at 119.9 ppm, is observed in the melamine-CNT complex, apart from the signals derived from oxidized-CNT and melamine. This additional resonance gives critical evidence for the strong interactions between melamine and CNT via C–N covalent bonds. Upon being thermally treated, the spectrum of g-C₃N₄ nanotubes presents two peaks located at 155.6 and 164.3 ppm, assigned to sp²-hybridized carbon in CN₂(NH_x) and the carbon atoms of CN₃ in the g-C₃N₄ networks, respectively.^{43,44} The spectrum of reduced CNTs is dominated by a broad peak, which can be recognized as a chemical shift anisotropy of the ¹³C nucleus.⁴² The peaks assigned to the oxygenated carbons cannot be observed, indicative of the sufficient elimination of the oxygen-containing functional groups on oxidized CNT spontaneously under high temperature. In addition, compared with the reduced CNTs, the g-C₃N₄-CNT shows a far broader resonance between 100 and 200 ppm, in which the characteristic signals originating from the g-C₃N₄ phase can be detected simultaneously, proving again the *in situ* covalent integration of g-C₃N₄ nanotubes onto CNTs.

Further evidence for the strong coupling between g-C₃N₄ and CNTs was achieved by measuring FT-IR spectra, Raman spectra, and fluorescence emission spectra. As analyzed in Figure S9, the formation of the g-C₃N₄-CNT complexes was disclosed in the FT-IR spectra by the integration of stretching vibrations of CNT (1570 cm⁻¹) and the breathing vibrations of triazine ring units (811 cm⁻¹). Raman spectra in Figure S10 show the shift of the G band position from 1579 to 1572 cm⁻¹ because of the covalent doping of g-C₃N₄ and the increase of the D/G intensity ratio from 1.06 to 1.18 owing to the structural disorder from the heteroatom incorporation, in comparison with that of CNTs. Additionally, the broadened D band in g-C₃N₄-CNT stems from multiple overlaps of C–N and C=N vibration modes from g-C₃N₄ and D band of CNTs. The complete quenching of fluorescence for g-C₃N₄-CNT with respect to the mechanical mixture of g-C₃N₄ nanotubes and CNTs clearly demonstrates that there is a much smoother electron-transfer channel between g-C₃N₄ and CNTs, which results from the C–N covalent coupling effect (Figure S11).

On the basis of the abovementioned covalently integrated g-C₃N₄-CNT, Pt was then loaded to demonstrate the effectiveness of this novel support toward anchoring high-quality extremely small-sized metal clusters. Transmission electron microscopy (TEM) was first carried out to examine the nanostructures and morphologies of the as-prepared Pt-g-C₃N₄-CNT. As illustrated in Figure S12 with wide range magnification, a well-defined 1D nanotube structure can be clearly observed. Close inspection from Figure 2c,d reveals that a thin enveloping layer of the g-C₃N₄ species is constructed on

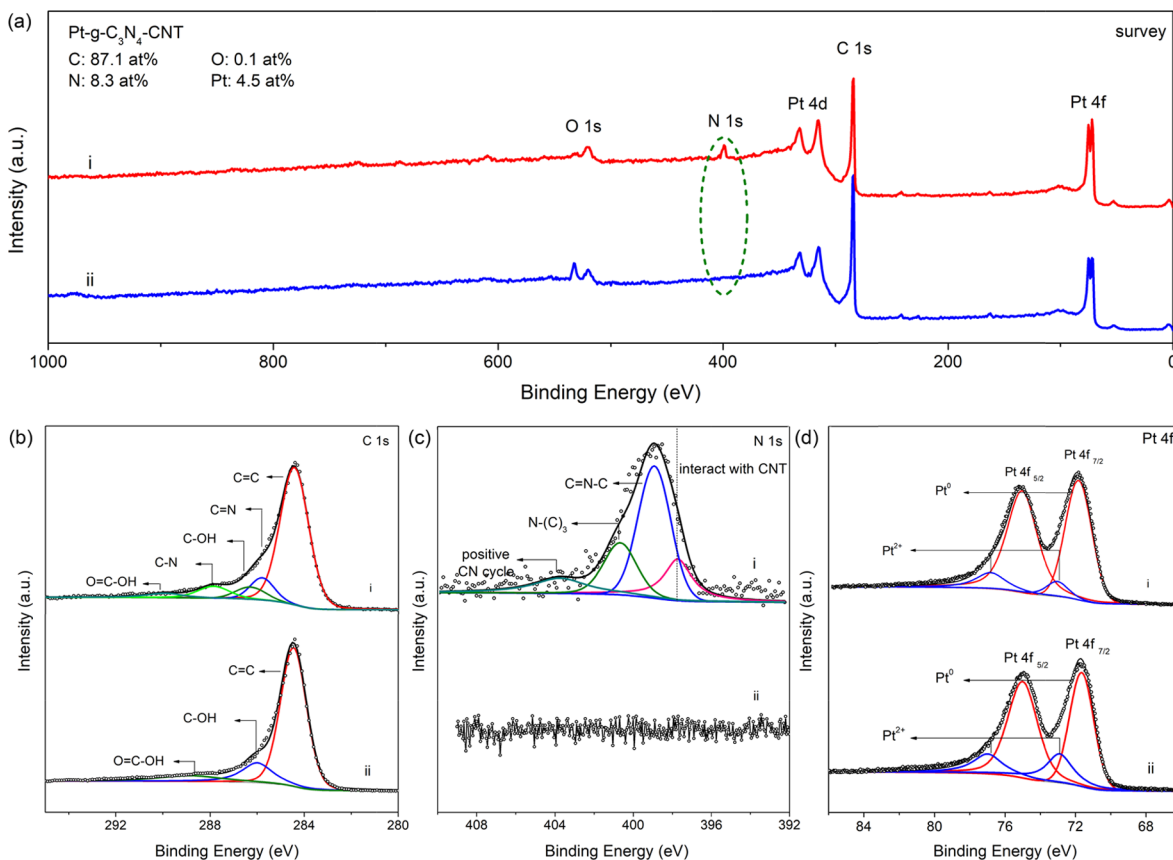


Figure 3. XPS analysis of the Pt-g-C₃N₄-CNT composites. (a) XPS survey spectra of (i) Pt-g-C₃N₄-CNT and (ii) Pt-CNT. High-resolution (b) C 1s, (c) N 1s, and (d) Pt 4f XPS spectra of (i) Pt-g-C₃N₄-CNT and (ii) Pt-CNT.

CNT, and numerous Pt clusters are homogeneously anchored onto the g-C₃N₄-CNT. The average diameter of these Pt clusters is counted to be 1.0 ± 0.2 nm (Figure S12c), and few clusters scatter out of the supports. This even distribution of the subnanometric Pt clusters is beneficial from the uniform N-coordinating cavities in g-C₃N₄-CNT structures, which could effectively tether Pt atoms and substantially enhance the interactions between Pt clusters and the support. After that, we also synthesized Pt-CNT and Pt-AC through similar preparation methods to Pt-g-C₃N₄-CNT except for varying the carbon supporting materials. As seen from Figure S13, it is found that the Pt components in these control samples show particle morphologies with larger size and easily form aggregates, mainly due to the chemical inertness of sp² carbon and their relatively weak interactions.⁶ To this point, the Pt-g-C₃N₄-CNT is able to offer more catalytic sites with almost identical Pt loading to the other kinds of Pt-carbon catalysts and possesses high resistance in avoiding the phenomena of agglomerating, dissolving, and Ostwald ripening that occur during the methanol oxidation reactions. The high-resolution TEM (HRTEM) images of Pt-g-C₃N₄-CNT in Figure 2e present a discernible lattice fringe with an interplanar spacing of 0.235 nm, assigned to the typical (111) planes in face-centred cubic (fcc) Pt crystals. In addition, the analysis of EELS element maps illustrates that the Pt-g-C₃N₄-CNT mainly comprises Pt, C, and N as effect constituents (Figure 2f); especially, all of these elements are highly dispersed across the whole nanotube.

The chemical and crystal structures of our Pt-g-C₃N₄-CNT composites were further studied by employing the powder X-

ray diffraction (XRD) analysis. The broad diffraction signal for Pt-g-C₃N₄-CNT ($2\theta = 26.5^\circ$) is between the typical (002) interlayer-stacking peak of CNT ($2\theta = 26.1^\circ$) and that of g-C₃N₄ ($2\theta = 27.4^\circ$), demonstrating the incorporation of g-C₃N₄ with CNT (Figure S14). The other three peaks at 39.8, 46.2, and 67.5° are indexed to the typical (111), (200), and (220) facets of crystallized Pt with fcc structures (JCPDS 04-0802). Importantly, the widening of these Pt diffraction peaks occurring in Pt-g-C₃N₄-CNT is due to the crystallite smallness effect, and the primary particle size of Pt-g-C₃N₄-CNT of 0.7 nm was also estimated from XRD Scherrer analysis. Compared with those of Pt-CNT (1.6 nm) and Pt-AC (2.3 nm), a significant reduction of the Pt particle size can be noticed, which is well coincident with the TEM analysis, proving again that the g-C₃N₄ component plays vital roles in reducing the size and stabilizing the noble metal clusters. In addition, the chemical states and detailed composition information of the Pt-g-C₃N₄-CNT were further analyzed through X-ray photo-electron spectroscopy (XPS). The typical evolution of the chemical states of Pt, C, and O is clearly detected in Figure 3a for both of the Pt-CNT and Pt-g-C₃N₄-CNT samples. No impurities were involved. Importantly, in the case of the Pt-g-C₃N₄-CNT, an obvious N signal corroborated the successful introduction of g-C₃N₄, and the corresponding N content was determined to be 8.3%, corresponding to 14.5% of g-C₃N₄ in the final product calculated with the C₃N₄ stoichiometry. The asymmetric C 1s spectra shown in Figure 3b can be deconvoluted into five peaks at 284.4, 285.8, 286.3, 287.9, and 290 eV, ascribed to the sp² C=C, sp² C=N, C-OH, sp³ C-N, and O=C-OH groups, respectively. The high-resolution

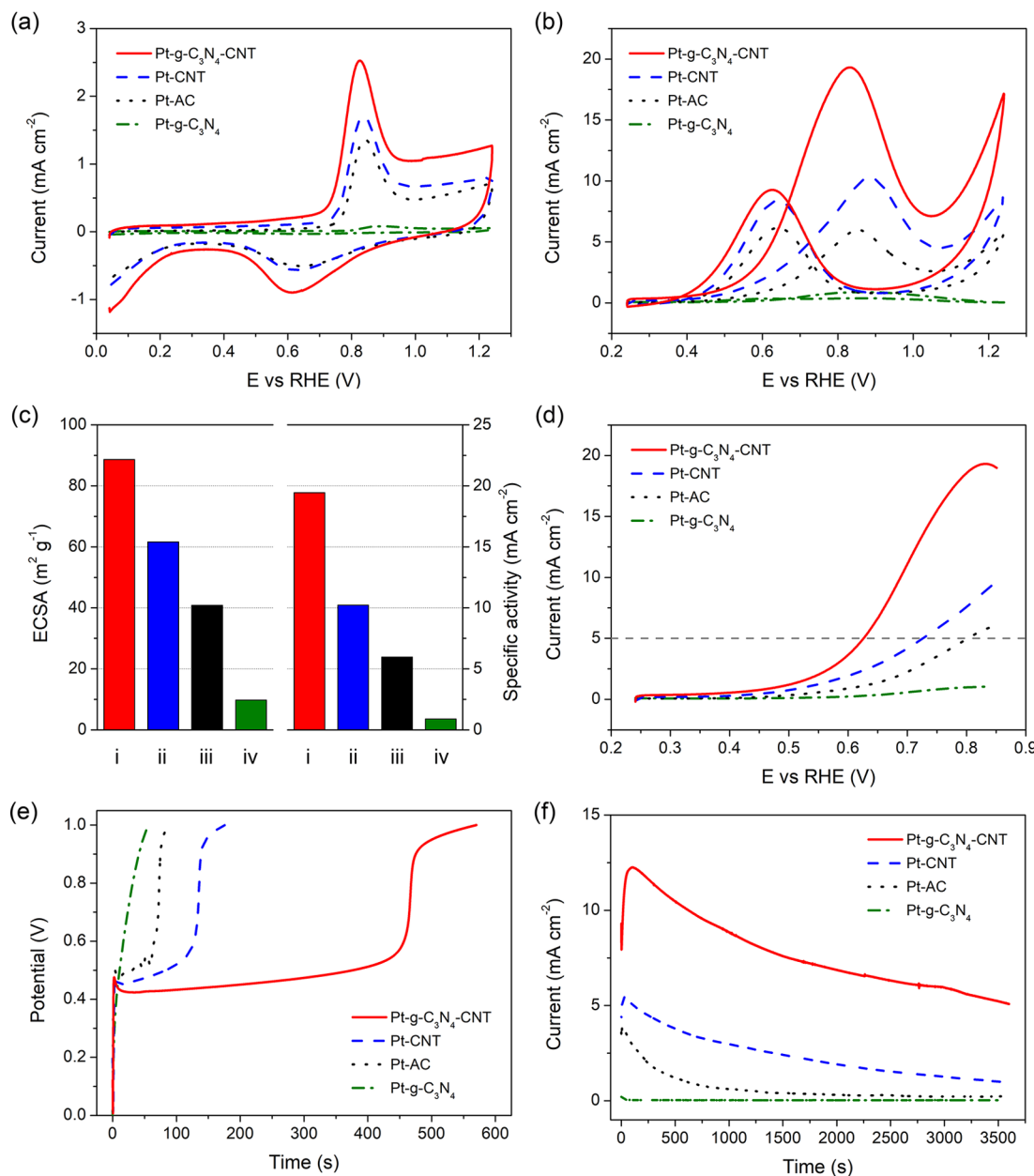


Figure 4. Electrocatalytic activities of Pt-g-C₃N₄-CNT composites toward methanol oxidation reactions. Cyclic voltammograms of Pt-g-C₃N₄-CNT in comparison with Pt-CNT, Pt-AC, and Pt-g-C₃N₄ in (a) 0.5 M H_2SO_4 solution and (b) 0.5 M H_2SO_4 with 1 M methanol solution at a scan rate of 20 mV s⁻¹. (c) ECSA values and specific activities for the catalysts of (i) Pt-g-C₃N₄-CNT, (ii) Pt-CNT, (iii) Pt-AC, and (iv) Pt-g-C₃N₄. (d) LSVs and (e) chronopotentiometric curves of Pt-g-C₃N₄-CNT, Pt-CNT, Pt-AC, and Pt-g-C₃N₄ in 0.5 M H_2SO_4 with 1 M methanol solution. (f) Chronoamperometric responses measured at 0.698 V (vs RHE) of Pt-g-C₃N₄-CNT, Pt-CNT, Pt-AC, and Pt-g-C₃N₄ in 0.5 M H_2SO_4 with 1 M methanol solution.

N 1s spectrum of Pt-g-C₃N₄-CNT reveals that four types of N bonding configurations coexist in this complex structures, including sp² N atoms in tri-s-triazine rings, bridging N atoms in N-(C)₃, and positively charged nitrogen in CN heterocycles and cyano groups centered at 398.8, 400.6, and 403.8 eV, respectively (Figure 3c). Herein, either the condensed tri-s-triazine N or CN heterocycles and cyano groups with lone electrons can serve as effective coordinating ligands and hence robustly anchor and stabilize Pt clusters. Note that both the binding energies and the relative intensities of the corresponding nitrogen species are well consistent with the g-C₃N₄ samples,⁷ giving strong evidence to demonstrate the incorporation of g-C₃N₄ layers on the surface of CNT. The

additional peak of pyridinic-N (397.7 eV) is observed attributing to the tough interactions between CNTs and N atoms in g-C₃N₄.⁴⁵ Moreover, the deconvolution of the Pt 4f spectra (Figure 3d) indicates that two intensive signals detected at 71.6 and 75.0 eV are attributed to the metallic Pt⁰, while the shoulder peaks located at 72.5 and 75.9 eV belong to the +2 oxidation Pt derived from the slight involvement of PtO phases. In comparison with Pt-CNT, the Pt-g-C₃N₄-CNT exhibits an obviously higher content of the metallic Pt component. It is because of the π -bonded planar g-C₃N₄ phases in the composite, which prominently immobilize the metallic Pt and simultaneously prevent the oxidation of Pt, similar to the amino effect reported elsewhere.^{46,47} As

Table 1. Compiled Studies Comparing the Electrochemical Performances Based on the CV Analysis for Different Catalysts

electrode	loading amount of Pt [mg·cm ⁻²]	ECSA [m ² ·g ⁻¹]	potential on I _F [V vs RHE]	I _F [mA·cm ⁻²]	I _R [mA·cm ⁻²]	I _F /I _R ratio
Pt-g-C ₃ N ₄ -CNT	0.0272	88.69	0.831	19.45	9.25	2.10
Pt-CNT	0.0276	61.63	0.885	10.23	8.40	1.22
Pt-AC	0.0291	40.82	0.853	5.97	6.17	0.97
Pt-g-C ₃ N ₄	0.0252	9.79	0.867	0.89	0.34	2.62

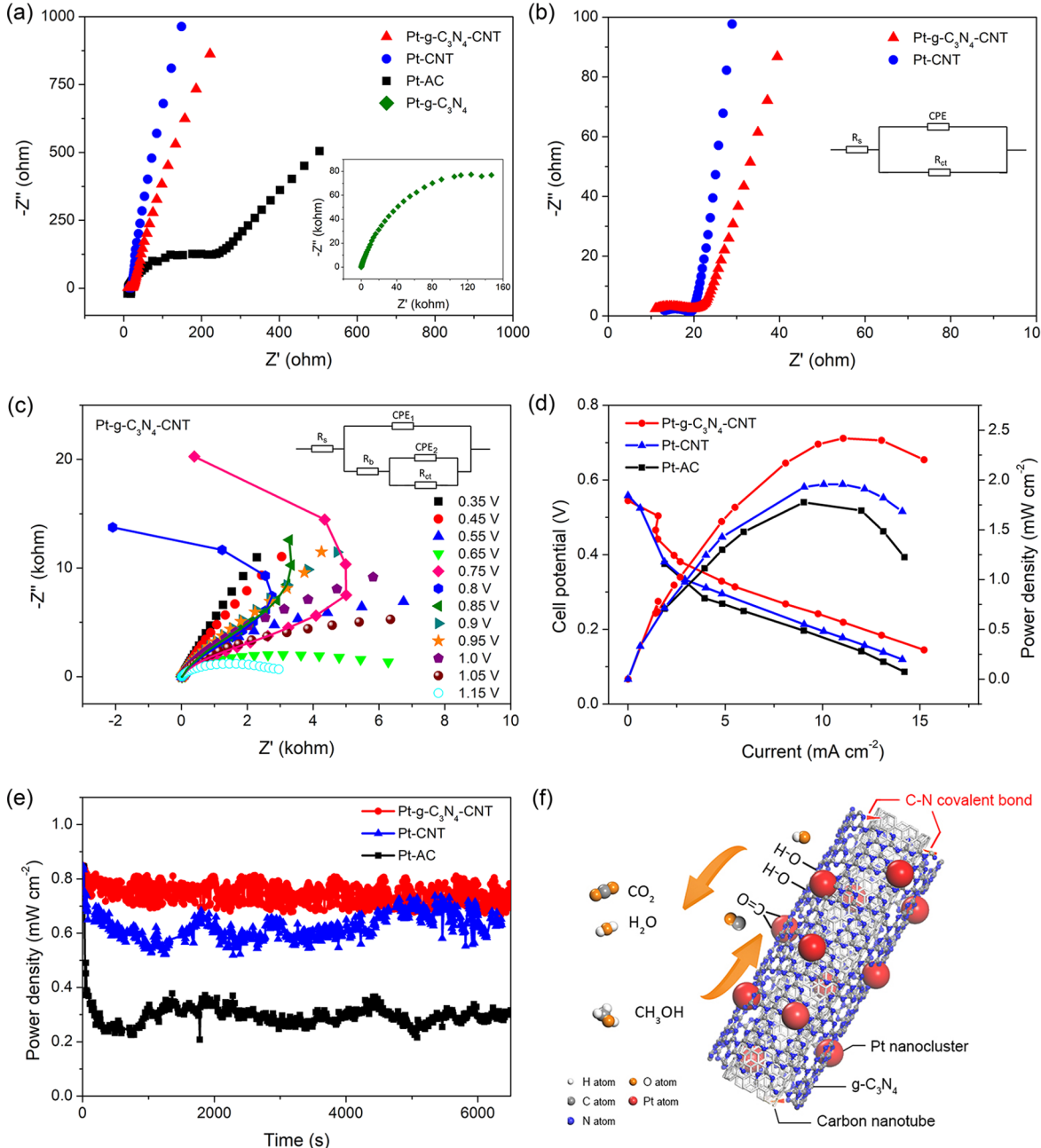


Figure 5. (a) Nyquist plots of EIS for Pt-g-C₃N₄-CNT, Pt-CNT, Pt-AC, and Pt-g-C₃N₄ in 0.5 M H₂SO₄ with 1 M methanol solution. (b) Local enlargement of the Nyquist plots for Pt-g-C₃N₄-CNT and Pt-CNT. The inset in panel (b) describes the equivalent circuits for fitting the impedance spectra. (c) Nyquist plots of EIS for methanol oxidation reaction on Pt-g-C₃N₄-CNT at various electrode potentials. The inset in panel (c) represents the equivalent circuit for the negative impedance. (d) Steady-state polarization curves, power-density curves, and (e) discharge curves at 0.35 V of the DMFCs using Pt-g-C₃N₄-CNT, Pt-CNT, and Pt-AC as anode catalysts with methanol (1 M) at 60 °C. (f) Schematic diagram of the methanol electrocatalytic processes on the Pt-g-C₃N₄-CNT catalyst.

considered, the more the metallic Pt, the better the electrocatalytic performances. Combining all the abovementioned measurements, it is reasonable to deduce that a g-C₃N₄ nanotube covalently functionalized CNT is successfully

fabricated, and the resulting g-C₃N₄-CNT support is able to productively trap and stabilize the subnanometric Pt clusters.

The electrocatalytic activity of the synthesized Pt-g-C₃N₄-CNT catalyst toward the methanol oxidation reaction was

evaluated and compared to those of Pt-CNT, Pt-AC, and Pt-g-C₃N₄ to validate theoretical predictions. The electrochemically active specific surface areas (ECSAs) of these catalysts were initially estimated by the method of cyclic voltammograms (CVs) in the electrolyte of 0.5 M H₂SO₄. Shown in Figure 4a, the distinctive potential regions are associated with the CO_{ad} stripping process between 0.8 and 1.0 V. Assuming that stripping a full monolayer of CO_{ad} on Pt catalysts consumes a charge of 420 μC cm⁻²⁴⁸, the ECSA values are calculated to be 88.69 m² g⁻¹ for Pt-g-C₃N₄-CNT, 61.63 m² g⁻¹ for Pt-CNT, 40.82 m² g⁻¹ for Pt-AC, and 9.79 m² g⁻¹ for Pt-g-C₃N₄. This implies that Pt-g-C₃N₄-CNT is more accessible to electrochemical aspects, which is crucial for electrocatalytic reactions. It should be noted that the extremely low ECSA values of Pt-g-C₃N₄ derive from the poor electrical conductivities owing to the intrinsic porous nature of g-C₃N₄. After that, the electrocatalytic performance toward methanol oxidation was evaluated by the polarization curves recorded in a N₂-saturated electrolyte containing 0.5 M H₂SO₄ and 1 M methanol solution (Figure 4b). The specific activity curves were plotted by aligning the current with the surface areas. As expected, the Pt-g-C₃N₄-CNT shows the highest methanol oxidation current densities up to 19.45 mA cm⁻², which is nearly 2- to 10-fold higher than those of Pt-CNT (10.23 mA cm⁻²), Pt-AC (5.97 mA cm⁻²), and Pt-g-C₃N₄ (0.89 mA cm⁻²) (Figure 4c) and recently state of the art Pt-based electrocatalysts, including Pt/RuO₂/graphene⁴⁹ (18.2 mA cm⁻²), Pt/graphene⁵⁰ (333.3 mA mg⁻¹), Pt/low-defect graphene⁵¹ (203.8 mA mg⁻¹), Pt/mesoporous carbon⁵² (450 mA mg⁻¹), Pt/N-doped mesoporous carbon⁵³ (360 mA mg⁻¹), Pt/N-doped graphene⁵⁴ (400 mA mg⁻¹), Pt/g-C₃N₄/porous graphene⁶ (612.8 mA mg⁻¹), FePtPd nanowires⁵⁵ (488.7 mA mg⁻¹), PtPd bimetallic nanodendrites⁵⁶ (490 mA mg⁻¹), PtAu nanodendrites/graphene⁵⁷ (365 mA mg⁻¹), and Pt/CdS quantum dots⁵⁸ (4.08 mA cm⁻²) (Table S2). Besides, the Pt-g-C₃N₄-CNT exhibits a lower onset potential (Figure 4d) and greater I_F/I_R ratio (Table 1), where the value of I_F is obtained from the forward scan and that of I_R is obtained from the reverse scan, compared with the other three catalysts, especially for the commercial Pt-AC. The onset potential toward methanol oxidation for the Pt-g-C₃N₄-CNT catalyst exhibits an evident negative shift, figuring out that the catalytic reactions are far easier to be initialized. The higher I_F/I_R ratio indicates that methanol sufficiently participated in the catalytic reactions after the forward scan, generating less poisoning intermediate products, thus managing higher tolerance to the accumulation of intermediate products (mainly CO_{ad})^{59,60}, consistent with the abovementioned theoretical forecast by the free energy diagram. To further confirm this point, chronopotentiometric tests were conducted, and the results are presented in Figure 4e. The potentials, monitored at a constant current, were gradually increased for all the electrodes as the test progresses. It is noted that our Pt-g-C₃N₄-CNT catalyst is able to sustain the voltage platform at a relatively low level for the longest period of ~570 s, more competitive than those of Pt-CNT (~170 s), Pt-AC (~90s), and Pt-g-C₃N₄ (~60 s), demonstrating that this unique configuration of Pt-g-C₃N₄-CNT architectures is more energetically favorable to eliminating the CO-like poisoning species from the electrode surfaces.

Other crucial issues that largely determine the usage of the catalysts are long-term stability and durability. We then performed chronoamperometric measurements of Pt-g-C₃N₄-CNT, Pt-CNT, Pt-AC, and Pt-g-C₃N₄ at a steady potential of

0.5 V. All the electrodes experience a similar condition of their electrocatalytic activities (Figure 4f), which shows an obvious activation stage and subsequently a pseudo-stable stage. After that, unavoidable current decays were observed arising from the following aspects, including the accumulation of intermediate carbonaceous products, the electrochemical corrosion of supporting materials, and the production of platinum oxides. Clearly, the Pt-g-C₃N₄-CNT shows both the tardiest current decays and the highest steady-state current densities among all the electrodes, indicating the best electrochemical durabilities for methanol oxidation across all the studied catalysts. Figure S15 shows the TEM image and the particle size distribution of the Pt-g-C₃N₄-CNT subjected to a durability experiment. Negligible deterioration in its structural integrity was observed, which is ascribed to the modification of the highly ordered and closely packed g-C₃N₄ layers and the strong coupling of g-C₃N₄ and CNT via the C–N covalent bond, providing enhanced anticorrosion abilities, thereby retaining the overall structures of this electrocatalyst. Additionally, the Pt clusters were still uniformly dispersed on the support and even slightly grew resulting from the Ostwald ripening during the harsh electrochemical process. Such a phenomenon can be clearly assigned to the strong interactions between Pt and g-C₃N₄-CNT support, which play crucial roles in anchoring Pt clusters firmly on the substrates; hence, the migration or agglomeration of these Pt clusters has been effectively suppressed, in good agreement with the DFT computation.

To further reveal the electrochemical properties of Pt-g-C₃N₄-CNT, electrochemical impedance spectroscopy (EIS) was carried out. As illustrated in Figure 5a,b, the Pt-g-C₃N₄-CNT possesses a relatively low charge transfer resistance, which shows a value of 17.1 Ω based on the analysis of the diameters of the semiarcs, obviously lower than those analyzed in the samples of Pt-AC (288 Ω) and Pt-g-C₃N₄ (\approx 260 kΩ) and close to that of Pt-CNT (11.2 Ω). Such good electrical conductivity is able to offer rapid kinetics toward the electrocatalytic process of methanol oxidation and significantly promote the improvement of the catalytic efficiency. Then the dynamics of methanol electrooxidation catalyzed by Pt-g-C₃N₄-CNT was investigated. Figure 5c shows the impedance spectra measured in 0.5 M H₂SO₄ with 1 M methanol solution at different electrode potentials. It can be seen that the diameters of the semiarcs initially reduce from a potential of 0.35 to 0.65 V, indicative of the enhanced electron-transfer rate for methanol oxidation reactions at higher potentials. By further increasing the potential, the negative impedance arises up, suggesting the introduction of (pseudo)-inductive characters in the impedance spectra resulting from the accumulation of chemisorbed hydroxyl (–OH) on the surfaces of the electrode.⁶¹ Combined with DFT computations, the electrooxidation of methanol on Pt goes through an indirect pathway, and the poisoning intermediate species are recognized mainly as adsorbed CO_{ad} species. However, the adsorbed CO_{ad} scarcely strips out until the oxygen-containing groups, that is, –OH, are produced on the Pt surface under high potentials. Considering that the g-C₃N₄, as one kind of metal-free catalyst, possesses efficient catalytic activities toward water splitting reactions, the incorporation of the g-C₃N₄ could accelerate the formation of adsorbed –OH species at a low electrode potential,^{7,62} thus promoting the process of oxidative removal of the adsorbed CO_{ad}. This process makes the Pt sites with less accumulation of CO_{ad}, which results in less CO_{ad} poisoning and assures sufficient catalytically active sites toward

the accession for the reactants. To demonstrate the potential of the Pt-g-C₃N₄-CNT catalyst in a DMFC, the catalysts were integrated at anodes of lab-made MEA fuel cells. Figure 5d presents the corresponding steady-state polarization curves as well as the power-density curves of the studied catalysts. Coinciding with the analysis from the above electrochemical measurements, the Pt-g-C₃N₄-CNT displays the highest power density of 2.5 mW cm⁻², which is more practical than those of Pt-CNT (1.9 mW cm⁻²), Pt-AC (1.7 mW cm⁻²), and the state of the art Pt/C commercial catalysts. Moreover, the Pt-g-C₃N₄-CNT exhibits the highly stable discharge abilities at 0.35 V (Figure 5e), which confirms the promising activity of Pt-g-C₃N₄-CNT for DMFC.

The engaging electrocatalytic properties of our Pt-g-C₃N₄-CNT composites with synergistic structural features can be attributable to these aspects. (i) The highly dispersed Pt nanoclusters with extremely small sizes can exploit the catalytic functions to the full, providing sufficient triple-phase boundaries and thus ensuring fast reaction kinetics toward methanol electrooxidation. (ii) The incorporation of g-C₃N₄ nanotubes first energetically reduces the activation energies of the methanol dehydrogenation processes and simultaneously facilitates accumulation of -OH species at relatively low potentials, thus accelerating the elimination of the adsorbed poisoning reaction intermediates (Figure 5f). Moreover, the high level of pyridinic nitrogen in the CN heterocyclic ring plays an important role in capturing and stabilizing subnanometric Pt clusters via strong metal-support interactions, which well act to tightly tether Pt clusters, effectively avoiding their migration and agglomeration upon the electrochemical tests. (iii) The covalent bonding between g-C₃N₄ and CNT significantly enhances the structural stability, renders the excellent anticorrosion ability of the catalytic system, and assists proton transportation upon the catalytic reactions. (iv) The CNT backbones afford innumerable ultrafast electronic conductive channels, remarkably promoting a rapid electron diffusion in the methanol oxidation reactions. In consequence, this novel Pt-g-C₃N₄-CNT electrocatalyst successfully integrates the respective merits of the individual components, holding great promising application in other high-performance energy storage and conversion devices.

In summary, we demonstrate a newly designed ternary nanocomposite consisting of Pt nanoclusters, g-C₃N₄ nanotubes, and CNT for promoting fuel-cell-related electrocatalysis. The as-obtained Pt-g-C₃N₄-CNT catalyst shows dramatically enhanced electrocatalytic abilities in terms of extraordinary electrocatalytic activities, excellent poison tolerances, and reliable long-term durability toward the methanol oxidation reactions, far superior to those of Pt-CNT or commercial Pt-AC catalysts. Physicochemical and electrochemical analysis combined with DFT calculation demonstrated that the chemical integration of g-C₃N₄ nanotubes on CNT plays a key role in optimizing the catalytic behavior of Pt catalysts for the multistep electrochemical reactions. Our study reveals that g-C₃N₄ could effectively uplift Pt's *d*-orbital position to the Fermi level, leading to the enhancement of the adsorption strength for reaction intermediates and the reduction of the energy barriers for the reaction pathways. Additionally, our investigations also suggest that g-C₃N₄ serving as a platform can decrease the size of Pt clusters and strengthen the metal-support interactions and as a cocatalyst can facilitate the accumulation of -OH species at a low potential, thus accelerating the elimination of the absorbed poisoning

intermediates. This molecular-level finding opens up new possibilities to design and develop more efficient and effective carbon-based supports to fabricate advanced heterogeneous catalysts and could also be extended to more applications in lithium-ion batteries, lithium-sulfur batteries, supercapacitors, and sensors.

■ ASSOCIATED CONTENT

§ Supporting Information

The Supporting Information is available free of charge on the ACS Publications website at DOI: 10.1021/acscatal.9b02987.

Detailed experiment section. Geometric structures of Pt on g-C₃N₄ and CNTs. Optimized structures of the intermediates on Pt-g-C₃N₄ and Pt-CNT. PDOS of Pt-CNT. Calculated Gibbs free energies of methanol oxidation reaction elementary steps. XRD, FT-IR, and SEM of supramolecular nanofiber. SEM and TEM of g-C₃N₄ nanotube. Raman and PL spectra of g-C₃N₄-CNT. XRD, TEM, and particle size distribution of Pt on g-C₃N₄-CNT, g-C₃N₄, CNT, and AC. TEM and particle size distribution of Pt-g-C₃N₄-CNT after the durability test (PDF)

■ AUTHOR INFORMATION

Corresponding Authors

*Email: fuyongsheng0925@163.com. fuyongsheng@njust.edu.cn (Y.F.).

*Email: aipingyu@uwaterloo.ca (A.Y.).

*Email: zhwchen@uwaterloo.ca (Z.C.).

ORCID

Aiping Yu: 0000-0002-7422-7537

Zhongwei Chen: 0000-0003-3463-5509

Notes

The authors declare no competing financial interest.

■ ACKNOWLEDGMENTS

This work is supported by the Natural Sciences and Engineering Research Council of Canada (NSERC), the Ontario Government for the Ontario Early Research Award Program, National Natural Science Foundation of China (Grant Nos. 51772156 and 51872144), China Postdoctoral Science Foundation (No. 2018 M640489), and PAPD of Jiangsu.

■ REFERENCES

- (1) Xu, S.; Kim, Y.; Park, J.; Higgins, D.; Shen, S.-J.; Schindler, P.; Thian, D.; Provine, J.; Torgersen, J.; Graf, T. Extending the limits of Pt/C catalysts with passivation-gas-incorporated atomic layer deposition. *Nat. Catal.* **2018**, *1*, 624.
- (2) Qiao, B.; Wang, A.; Yang, X.; Allard, L. F.; Jiang, Z.; Cui, Y.; Liu, J.; Li, J.; Zhang, T. Single-atom catalysis of CO oxidation using Pt₁/FeO_x. *Nat. Chem.* **2011**, *3*, 634.
- (3) Wang, A.; Li, J.; Zhang, T. Heterogeneous single-atom catalysis. *Nat. Rev. Chem.* **2018**, *2*, 65–81.
- (4) Sun, J.-K.; Kochovski, Z.; Zhang, W.-Y.; Kirmse, H.; Lu, Y.; Antonietti, M.; Yuan, J. General synthetic route toward highly dispersed metal clusters enabled by poly (ionic liquid)s. *J. Am. Chem. Soc.* **2017**, *139*, 8971–8976.
- (5) Zhu, C.; Fu, S.; Shi, Q.; Du, D.; Lin, Y. Single-atom electrocatalysts. *Angew. Chem., Int. Ed.* **2017**, *56*, 13944–13960.
- (6) Huang, H.; Yang, S.; Vajtai, R.; Wang, X.; Ajayan, P. M. Pt-decorated 3D architectures built from graphene and graphitic carbon

- nitride nanosheets as efficient methanol oxidation catalysts. *Adv. Mater.* **2014**, *26*, 5160–5165.
- (7) Zhang, W.; Fu, Y.; Wang, J.; Wang, X. 3D Hierarchically porous graphitic carbon nitride modified graphene-Pt hybrid as efficient methanol oxidation catalysts. *Adv. Mater. Interfaces* **2017**, *4*, 1601219.
- (8) Lin, C.-A. J.; Yang, T.-Y.; Lee, C.-H.; Huang, S. H.; Sperling, R. A.; Zanella, M.; Li, J. K.; Shen, J.-L.; Wang, H.-H.; Yeh, H.-I. Synthesis, characterization, and bioconjugation of fluorescent gold nanoclusters toward biological labeling applications. *ACS Nano* **2009**, *3*, 395–401.
- (9) Wang, S.; Meng, X.; Das, A.; Li, T.; Song, Y.; Cao, T.; Zhu, X.; Zhu, M.; Jin, R. A 200-fold quantum yield boost in the photoluminescence of silver-doped $\text{Ag}_{x}\text{Au}_{25-x}$ nanoclusters: the 13th silver atom matters. *Angew. Chem., Int. Ed.* **2014**, *53*, 2376–2380.
- (10) Gao, G.; Jiao, Y.; Waclawik, E. R.; Du, A. Single atom (Pd/Pt) supported on graphitic carbon nitride as an efficient photocatalyst for visible-light reduction of carbon dioxide. *J. Am. Chem. Soc.* **2016**, *138*, 6292–6297.
- (11) Zheng, Y.; Jiao, Y.; Zhu, Y.; Cai, Q.; Vasileff, A.; Li, L. H.; Han, Y.; Chen, Y.; Qiao, S.-Z. Molecule-level g-C₃N₄ coordinated transition metals as a new class of electrocatalysts for oxygen electrode reactions. *J. Am. Chem. Soc.* **2017**, *139*, 3336–3339.
- (12) Yang, X.-F.; Wang, A.; Qiao, B.; Li, J.; Liu, J.; Zhang, T. Single-atom catalysts: a new frontier in heterogeneous catalysis. *Acc. Chem. Res.* **2013**, *46*, 1740–1748.
- (13) Liu, L.; Lopez-Haro, M.; Lopes, C. W.; Li, C.; Concepcion, P.; Simonelli, L.; Calvino, J. J.; Corma, A. Regioselective generation and reactivity control of subnanometric platinum clusters in zeolites for high-temperature catalysis. *Nat. Mater.* **2019**, *18*, 866–873.
- (14) Wang, X.; Maeda, K.; Thomas, A.; Takanabe, K.; Xin, G.; Carlsson, J. M.; Domen, K.; Antonietti, M. A metal-free polymeric photocatalyst for hydrogen production from water under visible light. *Nat. Mater.* **2009**, *8*, 76–80.
- (15) Zhang, G.; Lin, L.; Li, G.; Zhang, Y.; Savateev, A.; Wang, X.; Antonietti, M. Ionothermal synthesis of triazine–heptazine-based copolymers with apparent quantum yields of 60% at 420 nm for solar hydrogen production from “Sea Water”. *Angew. Chem., Int. Ed.* **2018**, *57*, 9372–9376.
- (16) Zhang, G.; Lan, Z. A.; Wang, X. Conjugated polymers: catalysts for photocatalytic hydrogen evolution. *Angew. Chem., Int. Ed.* **2016**, *55*, 15712–15727.
- (17) Jiao, Y.; Zheng, Y.; Chen, P.; Jaroniec, M.; Qiao, S.-Z. Molecular scaffolding strategy with synergistic active centers to facilitate electrocatalytic CO₂ reduction to hydrocarbon/alcohol. *J. Am. Chem. Soc.* **2017**, *139*, 18093–18100.
- (18) Chen, Z.; Pronkin, S.; Fellinger, T.-P.; Kailasam, K.; Vilé, G.; Albani, D.; Krumeich, F.; Leary, R.; Barnard, J.; Thomas, J. M. Merging single-atom-dispersed silver and carbon nitride to a joint electronic system via copolymerization with silver tricyanomethanide. *ACS Nano* **2016**, *10*, 3166–3175.
- (19) Chen, Z.; Mitchell, S.; Vorobyeva, E.; Leary, R. K.; Hauert, R.; Furnival, T.; Ramasse, Q. M.; Thomas, J. M.; Midgley, P. A.; Dontsova, D. Stabilization of single metal atoms on graphitic carbon nitride. *Adv. Funct. Mater.* **2017**, *27*, 1605785.
- (20) Cao, Y.; Chen, S.; Luo, Q.; Yan, H.; Lin, Y.; Liu, W.; Cao, L.; Lu, J.; Yang, J.; Yao, T.; Wei, S. Atomic-level insight into optimizing the hydrogen evolution pathway over a Co₁-N₄ single-site photocatalyst. *Angew. Chem., Int. Ed.* **2017**, *129*, 12359–12364.
- (21) Chen, Z.; Zhao, J.; Cabrera, C. R.; Chen, Z. Computational screening of efficient single-atom catalysts based on graphitic carbon nitride (g-C₃N₄) for nitrogen electroreduction. *Small Methods* **2018**, *1800368*.
- (22) Li, X.; Cui, P.; Zhong, W.; Li, J.; Wang, X.; Wang, Z.; Jiang, J. Graphitic carbon nitride supported single-atom catalysts for efficient oxygen evolution reaction. *Chem. Commun.* **2016**, *52*, 13233–13236.
- (23) Zhu, J.; Sakaushi, K.; Clavel, G.; Shalom, M.; Antonietti, M.; Fellinger, T.-P. A general salt-templating method to fabricate vertically aligned graphitic carbon nanosheets and their metal carbide hybrids for superior lithium ion batteries and water splitting. *J. Am. Chem. Soc.* **2015**, *137*, 5480–5485.
- (24) Zheng, Y.; Jiao, Y.; Chen, J.; Liu, J.; Liang, J.; Du, A.; Zhang, W.; Zhu, Z.; Smith, S. C.; Jaroniec, M.; Lu, G. Q.; Qiao, S. Z. Nanoporous graphitic-C₃N₄@carbon metal-free electrocatalysts for highly efficient oxygen reduction. *J. Am. Chem. Soc.* **2011**, *133*, 20116–20119.
- (25) Fischer, A.; Antonietti, M.; Thomas, A. Growth confined by the nitrogen source: synthesis of pure metal nitride nanoparticles in mesoporous graphitic carbon nitride. *Adv. Mater.* **2007**, *19*, 264–267.
- (26) Groenewolt, M.; Antonietti, M. Synthesis of g-C₃N₄ nanoparticles in mesoporous silica host matrices. *Adv. Mater.* **2005**, *17*, 1789–1792.
- (27) Zhang, W.; Huang, H.; Li, F.; Deng, K.; Wang, X. Palladium nanoparticles supported on graphitic carbon nitride-modified reduced graphene oxide as highly efficient catalysts for formic acid and methanol electrooxidation. *J. Mater. Chem. A* **2014**, *2*, 19084–19094.
- (28) Zhang, W.; Fu, Y.; Liu, W.; Lim, L.; Wang, X.; Yu, A. A general approach for fabricating 3D MFe₂O₄ (M= Mn, Ni, Cu, Co)/graphitic carbon nitride covalently functionalized nitrogen-doped graphene nanocomposites as advanced anodes for lithium-ion batteries. *Nano Energy* **2019**, *57*, 48–56.
- (29) Han, Q.; Cheng, Z.; Gao, J.; Zhao, Y.; Zhang, Z.; Dai, L.; Qu, L. Mesh-on-mesh graphitic-C₃N₄@Graphene for highly efficient hydrogen evolution. *Adv. Funct. Mater.* **2017**, *27*, 1606352.
- (30) Yang, L.; Jiang, S.; Zhao, Y.; Zhu, L.; Chen, S.; Wang, X.; Wu, Q.; Ma, J.; Ma, Y.; Hu, Z. Boron-doped carbon nanotubes as metal-free electrocatalysts for the oxygen reduction reaction. *Angew. Chem., Int. Ed.* **2011**, *123*, 7270–7273.
- (31) Ma, T. Y.; Ran, J.; Dai, S.; Jaroniec, M.; Qiao, S. Z. Phosphorus-doped graphitic carbon nitrides grown in situ on carbon-fiber paper: flexible and reversible oxygen electrodes. *Angew. Chem., Int. Ed.* **2015**, *54*, 4646–4650.
- (32) Nørskov, J. K.; Rossmeisl, J.; Logadottir, A.; Lindqvist, L.; Kitchin, J. R.; Bligaard, T.; Jonsson, H. Origin of the overpotential for oxygen reduction at a fuel-cell cathode. *J. Phys. Chem. B* **2004**, *108*, 17886–17892.
- (33) Rossmeisl, J.; Qu, Z.-W.; Zhu, H.; Kroes, G.-J.; Nørskov, J. K. Electrolysis of water on oxide surfaces. *J. Electroanal. Chem.* **2007**, *607*, 83–89.
- (34) Feng, Q.; Zhao, S.; He, D.; Tian, S.; Gu, L.; Wen, X.; Chen, C.; Peng, Q.; Wang, D.; Li, Y. Strain engineering to enhance the electrooxidation performance of atomic-layer Pt on intermetallic Pt₃Ga. *J. Am. Chem. Soc.* **2018**, *140*, 2773–2776.
- (35) Paul, A.; Musgrave, C. B. A detailed theoretical study of the mechanism and energetics of methane to methanol conversion by cisplatin and catalytica. *Organometallics* **2007**, *26*, 793–809.
- (36) Ferrin, P.; Mavrikakis, M. Structure sensitivity of methanol electrooxidation on transition metals. *J. Am. Chem. Soc.* **2009**, *131*, 14381–14389.
- (37) Mavrikakis, M.; Hammer, B.; Nørskov, J. K. Effect of strain on the reactivity of metal surfaces. *Phys. Rev. Lett.* **1998**, *81*, 2819.
- (38) Gao, J.; Zhou, Y.; Li, Z.; Yan, S.; Wang, N.; Zou, Z. High-yield synthesis of millimetre-long, semiconducting carbon nitride nanotubes with intense photoluminescence emission and reproducible photoconductivity. *Nanoscale* **2012**, *4*, 3687–3692.
- (39) Zujovic, Z. D.; Laslau, C.; Bowmaker, G. A.; Kilmartin, P. A.; Webber, A. L.; Brown, S. P.; Travas-Sejdic, J. Role of aniline oligomeric nanosheets in the formation of polyaniline nanotubes. *Macromolecules* **2009**, *43*, 662–670.
- (40) Cai, W.; Piner, R. D.; Stadermann, F. J.; Park, S.; Shaibat, M. A.; Ishii, Y.; Yang, D.; Velamakanni, A.; An, S. J.; Stoller, M. Synthesis and solid-state NMR structural characterization of ¹³C-labeled graphite oxide. *Science* **2008**, *321*, 1815–1817.
- (41) Jeong, H.-K.; Lee, Y. P.; Lahaye, R. J.; Park, M.-H.; An, K. H.; Kim, I. J.; Yang, C.-W.; Park, C. Y.; Ruoff, R. S.; Lee, Y. H. Evidence of graphitic AB stacking order of graphite oxides. *J. Am. Chem. Soc.* **2008**, *130*, 1362–1366.

- (42) Stankovich, S.; Dikin, D. A.; Piner, R. D.; Kohlhaas, K. A.; Kleinhammes, A.; Jia, Y.; Wu, Y.; Nguyen, S. T.; Ruoff, R. S. Synthesis of graphene-based nanosheets via chemical reduction of exfoliated graphite oxide. *Carbon* **2007**, *45*, 1558–1565.
- (43) Cui, Y.; Ding, Z.; Fu, X.; Wang, X. Construction of conjugated carbon nitride nanoarchitectures in solution at low temperatures for photoredox catalysis. *Angew. Chem., Int. Ed.* **2012**, *51*, 11814–11818.
- (44) Sun, J.; Zhang, J.; Zhang, M.; Antonietti, M.; Fu, X.; Wang, X. Bioinspired hollow semiconductor nanospheres as photosynthetic nanoparticles. *Nat. Commun.* **2012**, *3*, 1139.
- (45) Liu, Q.; Zhang, J. Graphene supported Co-g-C₃N₄ as a novel metal–macrocyclic electrocatalyst for the oxygen reduction reaction in fuel cells. *Langmuir* **2013**, *29*, 3821–3828.
- (46) Wang, Y.; Yao, J.; Li, H.; Su, D.; Antonietti, M. Highly selective hydrogenation of phenol and derivatives over a Pd@ carbon nitride catalyst in aqueous media. *J. Am. Chem. Soc.* **2011**, *133*, 2362–2365.
- (47) Radkevich, V. Z.; Senko, T. L.; Wilson, K.; Grishenko, L. M.; Zaderko, A. N.; Diyuk, V. Y. The influence of surface functionalization of activated carbon on palladium dispersion and catalytic activity in hydrogen oxidation. *Appl. Catal., A* **2008**, *335*, 241–251.
- (48) Bockris, J. O. M.; Conway, B. E.; Yeager, E.; White, R. E. *Comprehensive Treatise of Electrochemistry*; Springer: 1985; Vol. 8.
- (49) Huang, H.; Zhu, J.; Li, D.; Shen, C.; Li, M.; Zhang, X.; Jiang, Q.; Zhang, J.; Wu, Y. Pt nanoparticles grown on 3D RuO₂-modified graphene architectures for highly efficient methanol oxidation. *J. Mater. Chem. A* **2017**, *5*, 4560–4567.
- (50) Wu, S.; Liu, J.; Tian, Z.; Cai, Y.; Ye, Y.; Yuan, Q.; Liang, C. Highly dispersed ultrafine Pt nanoparticles on reduced graphene oxide nanosheets: in situ sacrificial template synthesis and superior electrocatalytic performance for methanol oxidation. *ACS Appl. Mater. Interfaces* **2015**, *7*, 22935–22940.
- (51) Huang, H.; Chen, H.; Sun, D.; Wang, X. Graphene nanoplate-Pt composite as a high performance electrocatalyst for direct methanol fuel cells. *J. Power Sources* **2012**, *204*, 46–52.
- (52) Jiang, H.; Zhao, T.; Li, C.; Ma, J. Functional mesoporous carbon nanotubes and their integration in situ with metal nanocrystals for enhanced electrochemical performances. *Chem. Commun.* **2011**, *47*, 8590–8592.
- (53) Long, G.-F.; Li, X.-H.; Wan, K.; Liang, Z.-X.; Piao, J.-H.; Tsiakaras, P. Pt/CN-doped electrocatalysts: superior electrocatalytic activity for methanol oxidation reaction and mechanistic insight into interfacial enhancement. *Appl. Catal., B* **2017**, *203*, 541–548.
- (54) Xiong, B.; Zhou, Y.; Zhao, Y.; Wang, J.; Chen, X.; O’Hayre, R.; Shao, Z. The use of nitrogen-doped graphene supporting Pt nanoparticles as a catalyst for methanol electrocatalytic oxidation. *Carbon* **2013**, *52*, 181–192.
- (55) Guo, S.; Zhang, S.; Sun, X.; Sun, S. Synthesis of ultrathin FePtPd nanowires and their use as catalysts for methanol oxidation reaction. *J. Am. Chem. Soc.* **2011**, *133*, 15354–15357.
- (56) Wang, L.; Nemoto, Y.; Yamauchi, Y. Direct synthesis of spatially-controlled Pt-on-Pd bimetallic nanodendrites with superior electrocatalytic activity. *J. Am. Chem. Soc.* **2011**, *133*, 9674–9677.
- (57) Yuan, W.; Fan, X.; Cui, Z. M.; Chen, T.; Dong, Z.; Li, C. M. Controllably self-assembled graphene-supported Au@Pt bimetallic nanodendrites as superior electrocatalysts for methanol oxidation in direct methanol fuel cells. *J. Mater. Chem. A* **2016**, *4*, 7352–7364.
- (58) Zhai, C.; Zhu, M.; Pang, F.; Bin, D.; Lu, C.; Goh, M. C.; Yang, P.; Du, Y. High efficiency photoelectrocatalytic methanol oxidation on CdS quantum dots sensitized Pt electrode. *ACS Appl. Mater. Interfaces* **2016**, *8*, 5972–5980.
- (59) Cui, Z.; Chen, H.; Zhao, M.; Marshall, D.; Yu, Y.; Abruña, H.; DiSalvo, F. J. Synthesis of structurally ordered Pt₃Ti and Pt₃V nanoparticles as methanol oxidation catalysts. *J. Am. Chem. Soc.* **2014**, *136*, 10206–10209.
- (60) Huang, L.; Zhang, X.; Wang, Q.; Han, Y.; Fang, Y.; Dong, S. Shape-control of Pt-Ru nanocrystals: tuning surface structure for enhanced electrocatalytic methanol oxidation. *J. Am. Chem. Soc.* **2018**, *140*, 1142–1147.
- (61) Lu, Y.; Chen, W. PdAg alloy nanowires: facile one-step synthesis and high electrocatalytic activity for formic acid oxidation. *ACS Catal.* **2011**, *2*, 84–90.
- (62) Xu, J.; Cao, S.; Brenner, T.; Yang, X.; Yu, J.; Antonietti, M.; Shalom, M. Supramolecular chemistry in molten sulfur: preorganization effects leading to marked enhancement of carbon nitride photoelectrochemistry. *Adv. Funct. Mater.* **2015**, *25*, 6265–6271.